CHEMISTRY OF MATERIALS
Cite This: Chem. Mater. 2019, 31, 1370−1380
Article
pubs.acs.org/cm

# Facile One-Pot Synthesis of Pd@$Pt_{1L}$ Octahedra with Enhanced Activity and Durability toward Oxygen Reduction

Ming Zhou,[†,‡,§] Helan Wang,[†,+,§] Ahmed O. Elnabawy,[∥,§] Zachary D. Hood,[¶,#] Miaofang Chi,[#] Peng Xiao,[‡] Yunhuai Zhang,[‡] Manos Mavrikakis,*[,∥] and Younan Xia*[,†,¶]

[†]The Wallace H. Coulter Department of Biomedical Engineering, Georgia Institute of Technology and Emory University, Atlanta, Georgia 30332, United States

[∥]Department of Chemical and Biological Engineering, University of Wisconsin−Madison, Madison, Wisconsin 53706, United States

[‡]College of Chemistry and Chemical Engineering, Chongqing University, Chongqing 400044, China

[¶]School of Chemistry and Biochemistry, School of Chemical and Biomolecular Engineering, Georgia Institute of Technology, Atlanta, Georgia 30332, United States

[+]College of Chemistry, Chemical Engineering and Biotechnology, Donghua University, Shanghai 201620, China

[#]Center for Nanophase Materials Sciences Oak Ridge National Laboratory, Oak Ridge, Tennessee 37831, United States

Supporting Information

**ABSTRACT:** A successful strategy for reducing the content of Pt without compromising the activity of a Pt-based catalyst is to deposit Pt as an ultrathin overlayer on the surface of another metal. Here, we report a facile one-pot synthesis of Pd@$Pt_{1L}$ (1L: one atomic layer) core−shell octahedra using a solution-phase method. The success of this method relies on the use of metal precursors with markedly different reduction kinetics. In a typical synthesis, the ratio between the initial reduction rates of the Pd(II) and Pt(II) precursors differed by almost 100 times, favoring the formation of Pd−Pt bimetallic octahedra with a core−shell structure. The reduction of the Pt(II) precursor at a very slow rate and the use of a high temperature allowed the deposited Pt atoms to spread and cover the entire surface of Pd octahedral seeds formed in the initial stage. More importantly, we were able to scale up this synthesis using continuous-flow reactors without compromising product quality. Compared to a commercial Pt/C catalyst, the Pd@$Pt_{1L}$ core−shell octahedra showed major augmentation in terms of catalytic activity and durability for the oxygen reduction reaction (ORR). After 10000 cycles of accelerated durability test, the core−shell octahedra still exhibited a mass activity of 0.45 A $mg^{-1}_{Pt}$. We rationalized the experimental results using DFT calculations, including the mechanism of synthesis, ORR activities, and possible Pd−Pt atom swapping to enrich the outermost layer with Pd. Specifically, the as-synthesized Pd@$Pt_{1L}$ octahedra tended to take a slightly mixed surface composition because the deposited Pt atoms were able to substitute into Pd upon deposition on the edges; ORR energetics were more favorable on pure Pt shells as compared to significantly mixed Pd−Pt shells, and the activation energy barriers calculated for the Pd−Pt atom swapping were too prohibitive to significantly alter the surface composition of the as-synthesized Pd@$Pt_{1L}$ octahedra, helping sustain their activity for prolonged operation.

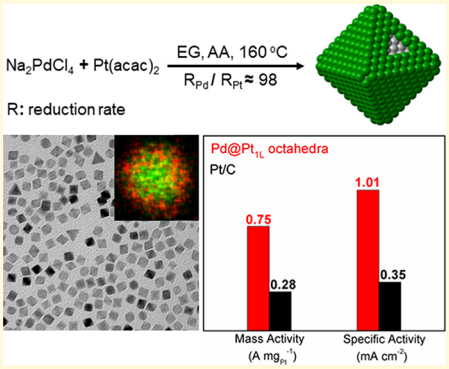




## INTRODUCTION

One of the major concerns about the proton exchange membrane fuel cells (PEMFCs) is the need to load a large amount of the Pt-based catalyst on the cathode to speed up the sluggish kinetics associated with the oxygen reduction reaction (ORR).[1−3] Given the low abundance, ever increasing cost, and sustainability issues associated with a precious metal such as Pt, it is not difficult to understand why it has been a challenging task to market the PEMFC technology on an industrial scale.[4−6] A viable strategy for mitigating this issue is to increase the utilization efficiency of Pt by engineering the surface structure through a facet-controlled synthesis and thereby reduce the Pt content.[7−9] To this end, various methods have been explored to improve the specific and mass activities of Pt-based catalysts.[10−13] One of the promising strategies is to deposit Pt atoms as a one-atom-thick shell on nanoparticles made of a more abundant and/or less expensive metal.[14−21] In particular, it has been demonstrated that monolayers or submonolayers of Pt could be deposited on nanoparticles made of Pd or other metals (as well as their alloys with Pt) via a galvanic replacement process that involves the underpotential deposition of the Cu shell.[15,16] Catalysts prepared using this approach showed greatly enhanced mass activity toward ORR. In addition, ultrathin skins of Pt were formed on the surfaces of

Received: November 14, 2018
Revised: January 17, 2019
Published: January 18, 2019




DOI: 10.1021/acs.chemmater.8b04756
Chem. Mater. 2019, 31, 1370−1380

nanoparticles made of $Pt_3Ni$, $Pt_3Co$, PtCu, or WC through annealing, dealloying, or high-temperature self-assembly to obtain catalysts with enhanced activities.[17−20] Most recently, our groups synthesized Pd@Pt core−shell nanocrystals featuring different surface structures through chemical deposition of Pt shells on Pd nanocrystal seeds with cubic, octahedral, and icosahedral shapes.[10,14,21] The thickness of the Pt shells could be increased from a few to six atomic layers, and catalysts based on the resultant core−shell nanocrystals showed significantly enhanced activity and durability when benchmarked against a state-of-the-art Pt/C catalyst. In general, it has been a challenging task to scale up the production of nanocrystal-based catalysts without compromising the quality control, although these prior studies have clearly validated the feasibility to generate advanced electrocatalysts by coating ultrathin Pt shells on nanocrystals made of another metal.

One-pot synthesis can potentially alleviate some of the issues associated with the quantity, time, and cost of a catalytic system. Owing to its promise for scale-up production, the one-pot route has received considerable interest.[22−24] In a recent demonstration, we established that Pt could be coated as conformal and uniform shells on Pd octahedral nanocrystals in a one-pot synthesis by quantitatively manipulating the ratio between the initial reduction rates of two precursors based upon $PdCl_4^{2-}$ and $PtCl_4^{2-}$.[25] When a relatively high reaction temperature of 160 °C was used, the deposited Pt atoms were able to diffuse across the entire surface of a Pd nanocrystal, generating a Pt shell through a layer-by-layer growth pathway. However, because the initial reduction rates of the two metal precursors only differed by about 10 times, it was difficult to obtain Pd@Pt core−shell nanocrystals with a monolayer or submonolayer coverage for the Pt shells. In separate studies, it was established that $Pt(acac)_2$ could be reduced at a much slower rate relative to that of $PtCl_4^{2-}$ owing to a relatively strong complexation of the acac ligand to $Pt^{2+}$.[26,27] As such, it is interesting to examine if one can generate Pt monolayer coating by replacing $PtCl_4^{2-}$ with $Pt(acac)_2$. In addition, it is more attractive to use $Pt(acac)_2$ rather than $PtCl_4^{2-}$ as the $Cl^-$ ions contained in the latter complex can facilitate oxidative etching, leading to a detrimental interdiffusion process between Pd and Pt atoms and thus the formation of alloys.[28] Taken together, it should be advantageous to extend the one-pot protocol by switching the precursor from $PtCl_4^{2-}$ to $Pt(acac)_2$ for the facile synthesis of $Pd@Pt_{1L}$ core−shell nanocrystals.

Herein, we demonstrate a one-pot method by judiciously choosing the right precursors for Pd and Pt to temporally separate their reduction into two steps, even though both of the precursors are presented in the same reaction solution. The success of our synthesis relies on the choice of two precursors with markedly different reduction rates. As such, by precisely manipulating the amount of the Pt precursor added, we are able to deterministically generate $Pd@Pt_{1L}$ core−shell nanocrystals with an octahedral shape for the development of ORR catalysts with substantially enhanced activities. More significantly, we have quantitatively analyzed the kinetics responsible for the formation of $Pd@Pt_{1L}$ core−shell nanocrystals. We are also able to scale up the synthesis using continuous-flow reactors without compromising the product quality. We augmented this with a DFT study of the diffusion mechanism of the deposited Pt atoms on the edges of Pd octahedra, as well as Pt−Pd swapping at the interface between the $Pt_{1L}$ shell and the Pd core. Our calculations explained the experimentally observed stability of the $Pd@Pt_{1L}$ core−shell octahedra.

## EXPERIMENTAL SECTION

**Chemicals and Materials.** While ethylene glycol (EG, lot no. L05B13) was ordered from J. T. Baker, all other chemicals, including sodium tetrachloropalladate(II) ($Na_2PdCl_4$, 99.998%), platinum(II) acetylacetonate [$Pt(acac)_2$, 98%], L-ascorbic acid (AA), poly(vinyl pyrrolidone) (PVP, MW = 55000), acetic acid (99.7%), hydrochloric acid (HCl, 37%), perchloric acid ($HClO_4$, 70%, PPT grade, Veritas), and ethanol (Pharmco Products, 200 proof), were purchased from Sigma-Aldrich. The chemicals were used as received. We used deionized (DI) water with a resistivity of 18.2 MΩ cm at room temperature to prepare all the aqueous solutions.

**Synthesis of $Pd@Pt_{1L}$ Core−Shell Octahedra.** The $Pd@Pt_{1L}$ octahedra were synthesized by adding a solution of $Na_2PdCl_4$ and $Pt(acac)_2$ in EG into another solution of PVP and AA in EG through the use of a pipet. In the standard protocol, 50 mg of AA and 50 mg of PVP were mixed in 7 mL of EG held in a vial at room temperature. The mixture was magnetically stirred for 10 min to ensure complete dissolution. Afterward, 3 mL of another solution (in EG) containing 38.2 mg of $Na_2PdCl_4$ and 15 mg of $Pt(acac)_2$ was injected with a pipet, and the final mixture was kept under magnetic stirring for another 10 min under ambient conditions. The mixture was then subjected to heating in an oil bath held at 160 °C. After 3 h, the vial was taken out and naturally cooled down to room temperature. Typically, we collected the product through centrifugation at 55000 rpm, followed by washing with acetone once and with DI water twice. The final solid was redispersed in 10 mL of DI water.

**Synthesis of $Pd@Pt_{1L}$ Core−Shell Octahedra in Continuous-Flow Reactors.** In a typical process, 38.2 mg of $Na_2PdCl_4$, 15 mg of $Pt(acac)_2$, 50 mg of AA, and 50 mg of PVP were mixed in 10 mL of EG hosted in a vial under ambient conditions with the assistance of magnetic stirring. The mixture was then heated to 80 °C for 10 min to ensure the dissolution of all the solids. Afterward, the solution was cooled down to room temperature prior to its introduction into a fluidic device that was assembled from a PTFE tube with an inner diameter of 1.58 mm (typically used at a length of 7.5 m), a syringe, and a syringe pump, as illustrated in Figure S1. In a standard protocol, the PTFE tube was immersed in an oil bath held at 160 °C and the fluidic system was operated at a flow rate of 0.3 mL $min^{-1}$. The residence time, defined by the length of the PTFE tube and the flow rate, was typically set to 30 min. The solution containing the solid products was collected in a centrifuge tube. After cooling down to room temperature, the solid products were precipitated out by adding 30 mL of acetone into 10 mL of as-obtained solution. After centrifugation at 12000 rpm for 10 min, the supernatant was discarded and the solid products were washed twice with water. The resulting $Pd@Pt_{1L}$ core−shell octahedra could be easily redispersed in 10 mL of water. Figure S2 shows a typical TEM image of the solid products. The Pd/Pt molar ratio for the $Pd@Pt_{1L}$ core−shell octahedra was 3.51, as indicated by ICP-MS analysis. All samples of $Pd@Pt_{1L}$ core−shell octahedra used for the electrochemical characterizations were produced using the fluidic system, unless otherwise mentioned.

**Quantitative Analysis of the Reaction Kinetics Involved in the Formation of the Core−Shell Octahedra.** The reduction rates of the Pd(II) and Pt(II) precursors were experimentally measured by analyzing the concentrations of the precursors remaining in the reaction solution after different periods of time. Such an analysis can be readily done with the assistance of an inductively coupled plasma mass spectrometer (NexION 300Q, PerkinElmer). In a typical protocol, we started the timer upon immersing the reaction container into an oil bath set to 160 °C. Using glass pipets, we constantly sampled aliquots of about 0.2 mL from the reaction solution at different points. The aliquots were quickly injected into 0.8 mL of aqueous KBr solution (500 mg $mL^{-1}$) kept at 0 °C to terminate the reduction. We then centrifuged the solution at 55000 rpm for 60 min to remove all the nanoparticles while keeping the


DOI: 10.1021/acs.chemmater.8b04756
Chem. Mater. 2019, 31, 1370−1380

Pd(II) and Pt(II) precursors in the supernatant. Prior to ICP-MS analysis, the supernatant was collected and diluted with 1% (v/v) aqueous $HNO_3$ solution to reach an ion concentration of about 100 ppb. From the ICP-MS data, we derived the rate constant ($k$) by performing a linear fit to the plot of ln[Pd(II)] or ln[Pt(II)] versus the reaction time. Once the rate constant was known, the instantaneous concentrations of the remaining Pd(II) or Pt(II) precursor could be calculated as a function of reaction time, if the reaction temperature was fixed.

**Instrumentation.** We took all TEM images on a Hitachi HT7700 (Hitachi, Tokyo, Japan) at an operation voltage of 120 kV. High-resolution high-angle annular dark-field scanning transmission electron microscopy (HAADF-STEM) and tomography images were captured on a JEOL JEM 2200FS STEM/TEM microscope equipped with a CEOS probe corrector (Heidelberg, Germany). Energy-dispersive X-ray (EDX) analysis was performed in STEM mode on an aberration-corrected JEOL 2200FS electron microscope equipped with a Bruker AXS SDD detector. The metal content, including the concentration of metal ions, in a sample was measured using ICP-MS analysis.

**Preparation of the Working Electrodes.** First, we loaded the as-prepared Pd@$Pt_{1L}$ core−shell octahedra on a carbon support (Ketjenblack EC-300J) at a metal content of 20% in terms of the total mass of Pd and Pt (based on ICP-MS analysis). Typically, we dispersed 2 mg of the Pd@$Pt_{1L}$ core−shell octahedra and 8 mg of Ketjenblack in 8 mL of ethanol under ultrasonication for about 4 h. We then collected the carbon-supported Pd@$Pt_{1L}$ octahedra using centrifugation, redispersed them in 10 mL of acetic acid, and heated the mixture at 60 °C for 10 h to help remove the chemical species adsorbed on the surface of the metal particles. Finally, the catalyst was collected through centrifugation and washed six times with ethanol. Once dried in an oven, we redispersed 3 mg of the catalyst in a mixture of 1 mL of isopropanol, 1 mL of DI water, and 40 $\mu$L of 5% Nafion under ultrasonication for about 60 min. We then placed 10 $\mu$L of the suspension on a precleaned glassy carbon rotating disk electrode (RDE, Pine Research Instrumentation) and dried the sample under ambient conditions. The RDE had a geometric area of 0.196 $cm^2$. We used the Pt/C catalyst from Tanaka Kikinzoku Kogyo K.K. as a benchmark for comparison. This state-of-the-art catalyst contained 46.1 wt % 2.8 nm Pt nanoparticles supported on Ketjenblack EC-300J. We dispersed 2 mg of the Pt/C catalyst in a mixture of 1 mL of isopropanol, 1 mL of DI water, and 40 $\mu$L of 5% Nafion under ultrasonication for about 60 min to produce an ink. We then placed 10 $\mu$L of the ink on a precleaned glassy carbon RDE and let the sample dry under ambient conditions.

**Electrochemical Measurements.** We conducted all the electrochemical measurements using a glassy carbon RDE connected to a CHI 600E potentiostat (CH Instruments). We used HydroFlex as the hydrogen reference electrode (Gaskatel) and a Pt mesh as the counter electrode. Typically, all potentials were converted to values in reference to the reversible hydrogen electrode (RHE), or $V_{RHE}$. The 0.1 M $HClO_4$ electrolyte was prepared by diluting a 70% stock solution with DI water, with the CV curve being recorded at room temperature in a $N_2$-saturated 0.1 M $HClO_4$ solution in the potential range of 0.08−1.10 $V_{RHE}$ at a scanning rate of 50 mV $s^{-1}$. We derived the specific electrochemical active surface area (ECSA) of each catalyst from the average charges associated with hydrogen adsorption and desorption in the region of 0.08−0.43 $V_{RHE}$ by taking a reference value of 240 $\mu$C $cm^{-2}$ (for Pd@$Pt_{1L}$ octahedra) for the complete desorption of a monolayer of hydrogen from the Pt(111) surface. The ORR activity of each catalyst was measured in an $O_2$-saturated 0.1 M $HClO_4$ solution at room temperature in the potential range of 0.08−1.10 $V_{RHE}$, typically at a scanning rate of 10 mV $s^{-1}$ and a rotating speed of 1600 rpm. We corrected the ORR data using ohmic $iR$ drop compensation. For the accelerated durability test, CVs and ORR polarization curves were recorded after sweeping the catalyst in an $O_2$-saturated 0.1 M $HClO_4$ solution at room temperature for 5000 and 10000 cycles in the range of 0.6 and 1.1 $V_{RHE}$ at a rate of 0.1 V $s^{-1}$.

**DFT Calculations.** We performed plane wave DFT calculations employing the projector augmented wave potentials[29,30] and the GGA-PW91 exchange correlation functional,[31] as realized in the Vienna ab initio simulation package.[32,33] We expanded the Kohn−Sham electron wave function in a plane wave basis set with a kinetic energy cutoff of 400 eV. The lattice constant of bulk Pd was calculated to be 3.96 Å, in agreement with the experimental value of 3.89 Å.[34]

**Metal Atom Diffusion on Edge Model.** Similar to our recent work,[35] we created an edge model by symmetrically eliminating a total of 40 atoms out of the top layers of an eight-layer Pd(110) slab of a 5 × 4 unit cell, to expose two adjacent {111} facets on either side of the edge. We then removed the edge atoms to expose the {110} facet at the interface between the two {111} planes, as shown in Figure S3. Therefore, this model is an accurate representation of the edges of the as-synthesized nanocrystals, as depicted in Figure 5A. The bottom two layers were fixed at their bulk positions, while the remainder of the atoms were allowed to fully relax. A Monkhorst−Pack $k$-point mesh of 1 × 2 × 1 was used to sample the Brillouin zone.[36] Activation energy barriers of diffusion of Pt atoms on the Pd edge model were calculated using the climbing-image nudged elastic band (CI-NEB) method,[37] with seven intermediate images interpolated between the initial and final states. Each image was converged to less than 0.10 eV $Å^{-1}$ calculated force on all atoms.

**Slab Calculations and Surface Segregation.** To model the ORR on octahedral nanocrystals, we performed calculations for the adsorption of O and OH on periodic (2 × 2) unit cells, representing a coverage of 0.25 ML. All slabs exposed the {111} facet and were five atomic layers thick, with the bottom two layers fixed and the remainder of the atoms (including the adsorbates) allowed to fully relax. Approximately, vacuum of 14 Å thick was used to separate the vertical images of the slab to avoid unphysical interactions in the $z$-direction. Adsorption was only allowed for the top surface of the slabs, with the inclusion of appropriate dipole correction to the electrostatic potential.[38,39] To capture small differences in energetics, we sampled the Brillouin zone using a dense Monkhorst−Pack $k$-point mesh of 10 × 10 × 1[36] and converged geometric optimizations to 0.01 eV $Å^{-1}$ Hellmann−Feynman interatomic forces. We performed these calculations on slabs representing the Pd and Pd@$Pt_{1L}$ core−shell in which the atoms of the top atomic layer of the Pd slab were replaced with Pt atoms.

As revealed by the EDX line scans for the Pd@$Pt_{1L}$ octahedral nanocrystals, a mixed Pd−Pt composition might be possible for the surface layers. Therefore, we permuted the Pt atoms among the top two layers to yield top layer compositions of 0, 25, 50, 75, and 100% of Pt atoms for the slab models representing the Pd@$Pt_{1L}$ core−shell octahedra, with the remaining Pt atoms located in the immediate subsurface layer. All these different Pd@$Pt_{1L}$ core−shell slab models are designed at the lattice constant of Pd, given that Pt is the minority species. In Table S1, we compare the total energies of these different slab configurations in vacuum and in the presence of 0.25 ML coverage of O or OH. Consistent with the literature,[40] we have found that Pt prefers to occupy the subsurface in vacuum, giving a 0% Pt composition for the top layer in the absence of any adsorbates (see Table S1). On the other hand, O and OH were both found to prefer a mixed surface layer composition, specifically, of 50% Pt under 0.25 ML of O and 25% Pt under 0.25 ML of OH. In the case of mixed compositions of the surface layer, O and OH were directly adsorbed to the Pt atom(s).

**Calculations of ORR Activities on Slab Models.** Gibbs free energies of gas-phase species (i.e., $H_2O$) and surface species (i.e., O and OH) were calculated as $G = E + ZPE - TS$, where $E$ is the total electronic energy, ZPE is the zero-point energy, $T$ is the absolute temperature of 298.15 K, and $S$ is entropy. Both $S$ and ZPE were estimated from the translational, vibrational, and rotational modes in the context of vibrational frequency calculations. The vibrational frequencies were estimated through numerical (i.e., finite difference approximation) second-order differentiation of forces with a step size of 0.015 Å, within the framework of harmonic oscillator approximation. To take into account the applied bias in electrochemical measurements, we employed the computational RHE approach of Nørskov and co-workers.[41] The reference electrode for this approach is the RHE, at which protons and electrons are in


DOI: 10.1021/acs.chemmater.8b04756
Chem. Mater. 2019, 31, 1370−1380

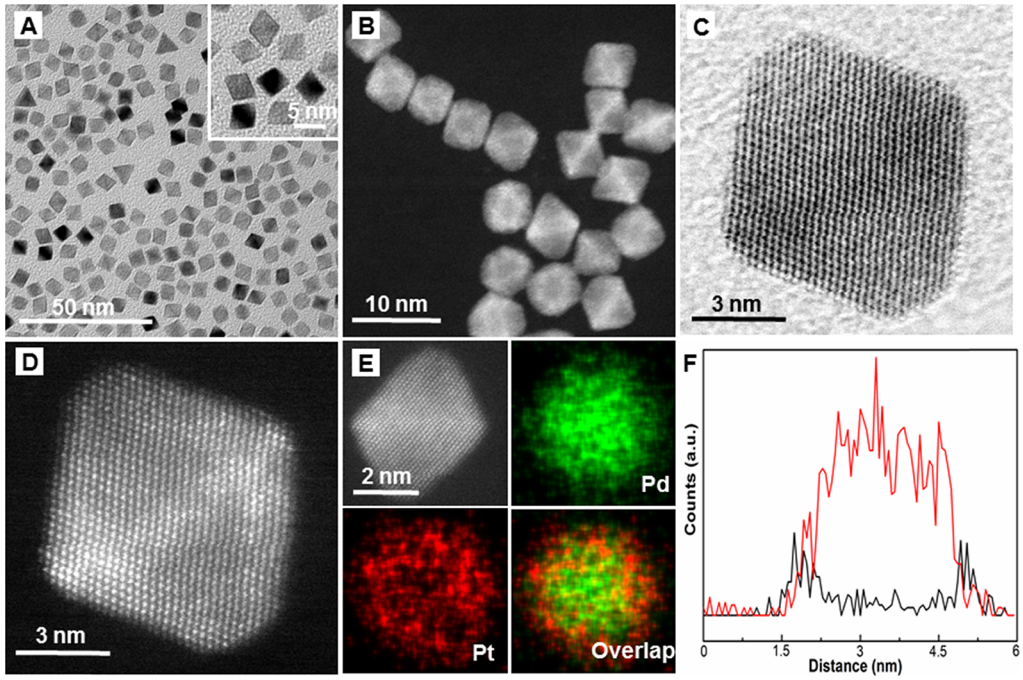


**Figure 1.** (A) TEM and (B) low-magnification HAADF-STEM images of Pd@$Pt_{1L}$ octahedral nanocrystals. (C) Bright-field STEM and (D) atomic-resolution HAADF-STEM images taken from an individual Pd@$Pt_{1L}$ octahedron. (E) HAADF-STEM image of a Pd@$Pt_{1L}$ octahedron and the corresponding EDX mapping of Pd and Pt. (F) EDX line scans of Pd (red trace) and Pt (black trace) recorded from a Pd@$Pt_{1L}$ octahedron.

thermodynamic equilibrium with hydrogen gas at a defined potential of 0.0 V, all pH, and standard conditions of temperature (298.15 K) and pressure (1 atm). Therefore, by definition, $\Delta G$ = 0.00 for $1/2H_2(g) \leftrightarrow H^+ + e^-$ at 0.0 $V_{RHE}$. This means that the free energy of a proton−electron pair equals half of that of hydrogen gas [$(H_2(g)]$ as calculated by DFT at 0.0 $V_{RHE}$. To modify the free energy in response to applied electrochemical bias ($U$), the free energy change of an electron is calculated as $-|e|U$, where $|e|$ is the absolute charge of an electron. In sum, the free energy change of either of our electrochemical steps [$O + H^+ + e^- \rightarrow OH$ and $OH + H^+ + e^- \rightarrow H_2O(g)$] is calculated as $\Delta G = \Delta E + \Delta ZPE - T\Delta S + |e|U$. Therefore, both electrochemical steps become more endothermic at more positive potentials (or bias). Given that we did not include a water bilayer in our model for computational convenience, we stabilized the free energy of adsorbed OH by 0.50 eV, whereas no stabilization was considered for adsorbed O, consistent with the literature.[42]

**Calculations of the Mechanism of Surface Segregation.** To rationalize the activity loss during the accelerated durability test and given the thermodynamic propensity of Pd to at least partially segregate to the top metal layer (see Table S1), we performed a detailed study of the mechanism by which a surface Pt atom can swap positions with a Pd atom in the immediate subsurface layer. Specifically, we performed such a study for slabs in vacuum and in the presence of 0.25 ML of O or OH. Furthermore, we calculated the swapping activation energy barriers (calculated via CI-NEB) up to a surface composition of 75% Pd,[37] given that O and OH are destabilized on pure Pd surface layers (Table S1). We have found that four-body rotations (which involve two top-layer metal atoms and two subsurface metal atoms) are less energetically favorable, and therefore, we only report the activation energy barriers of three-body rotations. We typically found multiple local minima along the trajectory of the minimum energy path (MEP) for this mechanism. In such cases, the MEP was broken down to intermediate pieces connecting the initial state, final state, and all local minima in between. The reported $E_a$ is the activation energy of the most difficult intermediate piece of the MEP, while the reported $\Delta E$ is simply the difference in total energy of the final state and the initial state.

## RESULTS AND DISCUSSION

In a standard batch synthesis of the Pd@$Pt_{1L}$ core−shell octahedra, $Na_2PdCl_4$ and $Pt(acac)_2$ were codissolved in EG and then added into another solution of PVP and AA in EG at room temperature through the use of a pipet. After the reaction was continued at 160 °C for 3 h, we obtained the core−shell octahedra. Figure 1A,B shows the TEM and HAADF-STEM images of the as-synthesized core−shell octahedra with an average edge length of 6.7 ± 0.4 nm, together with good uniformity in terms of both size and shape. Figure 1C,D shows bright-field and atomic-resolution HAADF-STEM images taken from an individual octahedron. These images indicate that the nanocrystals were dominated by {111} facets on the side faces, together with much smaller {100} facets at the slightly truncated corners. The large difference in atomic number between the two elements involved led to a contrast between the Pt shell and the Pd core. More importantly, these images suggest that the Pt shell only had a thickness of about one atomic layer. We also used ICP-MS to analyze the average number of Pt atomic layers in each core−shell nanocrystal and obtained a value of 0.95. Unless otherwise specified, we exclusively use the data derived from ICP-MS in the following discussion because this number reflects the average value for a large number of particles. We also confirmed the formation of a core−shell structure by analyzing the nanocrystal through the use of EDX mapping (Figure 1E). According to ICP-MS analysis, the Pd/Pt molar ratio was 3.53 for the Pd@$Pt_{1L}$ core−shell octahedra, which was almost identical to the value of 3.42 derived from the molar feeding ratio set for the Pd(II) and Pt(II) precursors. This result suggests that the conversion of both the Pd(II) and Pt(II) precursors could reach a level of >97% when both AA and EG were employed as the reductants.[25] Figure 1F shows the EDX line scans across an individual octahedron, confirming


DOI: 10.1021/acs.chemmater.8b04756
Chem. Mater. 2019, 31, 1370−1380

that Pt and Pd were mostly detected from the shell and core regions of the nanocrystal, respectively.

To elucidate how the core−shell octahedra were formed in our system, we analyzed the products sampled at different stages of a batch synthesis by TEM and ICP-MS. In this case, aliquots were taken out from the reaction mixture at different time points of a standard synthesis. Figure 2A−D shows TEM

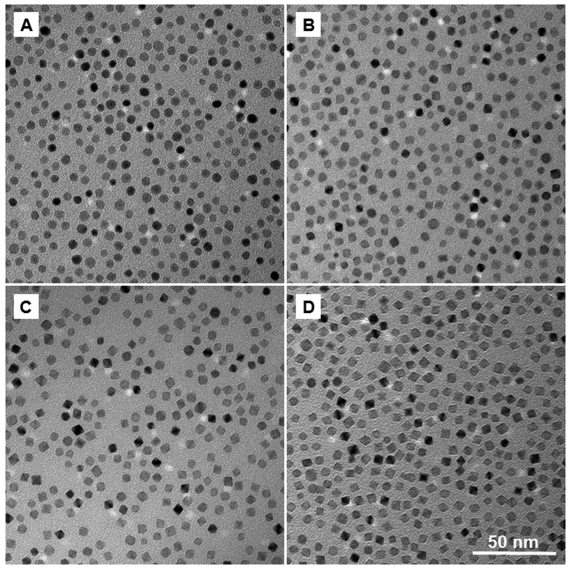


**Figure 2.** TEM images of the Pd@$Pt_{1L}$ octahedral nanocrystals synthesized using the standard protocol except for the difference in reaction time: (A) 2, (B) 20, (C) 60, and (D) 120 min.

images of the nanocrystals obtained at different intervals after the reaction container had been immersed in the oil bath held at 160 °C. At $t$ = 2 min, truncated octahedral nanocrystals with an average edge length of 6.0 ± 0.4 nm were formed (Figure 2A). After another 18 min, the nanocrystals had been transformed into an octahedral shape (Figure 2B). This result suggests that the growth largely occurred along the <100> directions in the initial stage of the synthesis because the {100} facets have a higher surface free energy than the {111} facets. Once the nanocrystals had evolved into an octahedral shape largely encased by {111} facets, the shape tended to stay as the reaction time was prolonged. As shown in Figure 2C,D, the edge length gradually increased from 6.2 ± 0.3 nm at $t$ = 20 min to 6.5 ± 0.2 and 6.7 ± 0.4 nm for $t$ = 60 and 120 min, respectively.

We further measured the changes in the Pt/Pd atomic ratio during the synthesis by ICP-MS. As shown in Figure 3, the Pt/Pd ratio was only 0.03 for the products obtained at $t$ = 2 min, suggesting that only the Pd(II) precursor had been reduced to form Pd truncated octahedral seeds. Afterward, the Pt/Pd ratio of the resultant products increased to 0.55 as the reaction time was increased to 180 min. Both the electron microscopy images and ICP-MS results clearly confirm that the core−shell nanocrystals are sequentially formed through the formation of Pd core first, followed by the deposition of a Pt overlayer. In a control experiment, only Pd truncated octahedra were observed when no Pt(II) precursor was added into the standard synthesis (Figure S4A). This result was also consistent with the products obtained in Figure 2A. In this case, Pd@$Pt_{1L}$ core−shell octahedra could still be formed when we introduced the $Pt(acac)_2$ precursor into the reaction

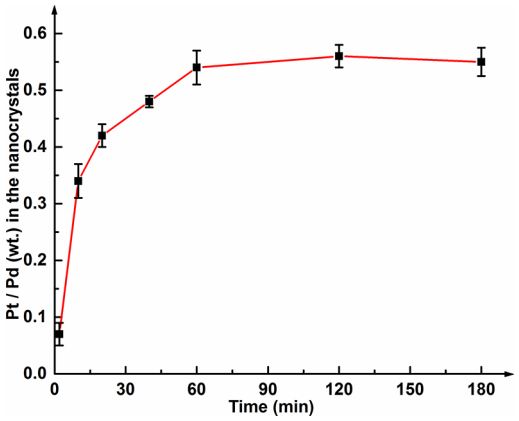


**Figure 3.** Plot showing the mass ratio of Pt to Pd determined using ICP-MS analysis as a function of reaction time for the samples shown in Figure 2.

system at $t$ = 1 h after almost all the Pd(II) precursor had been reduced (Figure S4B). These observations support our anticipation that $PdCl_4^{2-}$ was reduced at a much faster rate than $Pt(acac)_2$ under the same conditions. This difference in reduction rate can be largely attributed to the stronger complexation between the acetylacetone ligand and $Pt^{2+}$ and thereby a lower reduction potential.[26,27] Taken together, we can conclude that the core−shell nanocrystals were formed through the initial nucleation and growth of Pd octahedral nanocrystals, which then served as seeds for the deposition of Pt overlayers.

We believe that the temporal separation between the reduction of Pd(II) and Pt(II) precursors, due to the large difference in reduction kinetics, is a key factor in promoting the formation of a core−shell structure. To gain insights into the reduction kinetics of the synthesis, we analyzed the percentage of metal ions remaining in the reaction solution as a function of reaction time using ICP-MS and then derived the rate law. In general, the reduction of a salt precursor should follow the second-order rate law owing to the requirement of collision and then electron transfer between the precursor and reductant species.[43] In the present work, the amount of the reductant was used in large excess relative to that of the precursor, so the concentration of the reductant was supposed to change very little during the entire synthesis. As a result, it is not unreasonable to approximate the reduction kinetics as a pseudo-first-order reaction. Figure 4A,B shows the plots of ln[Pt(II)] and ln[Pd(II)] as a function of reaction time for the standard synthesis conducted at 160 °C. As expected, the values of $\ln[Pt(II)]_t$ and $\ln[Pd(II)]_t$ indeed decreased linearly with the reaction time, confirming that the reduction was first-order with respect to the precursor concentration. From the slopes of the linear regression lines, we obtained rate constants of $6.4 \times 10^{-4}$ and $1.8 \times 10^{-2}$ $s^{-1}$ for the Pt(II) and Pd(II) precursors, respectively, when the reduction was performed by a mixture of EG and AA. We repeated the kinetic measurement two more times to obtain the average reduction rate constants. We obtained rate constants of $6.40 \times 10^{-4}$, $6.42 \times 10^{-4}$, and $6.38 \times 10^{-4}$ $s^{-1}$ for the Pt(II) precursor, which gave a standard deviation of $1.60 \times 10^{-6}$. Similarly, the standard deviation for the rate constant of the Pd(II) precursor was determined to be $1.29 \times 10^{-4}$. From these data, it can be concluded that the measurements were reasonably accurate. The ratio between the rate constants for the Pt(II) and Pd(II) precursors was only


DOI: 10.1021/acs.chemmater.8b04756
Chem. Mater. 2019, 31, 1370−1380

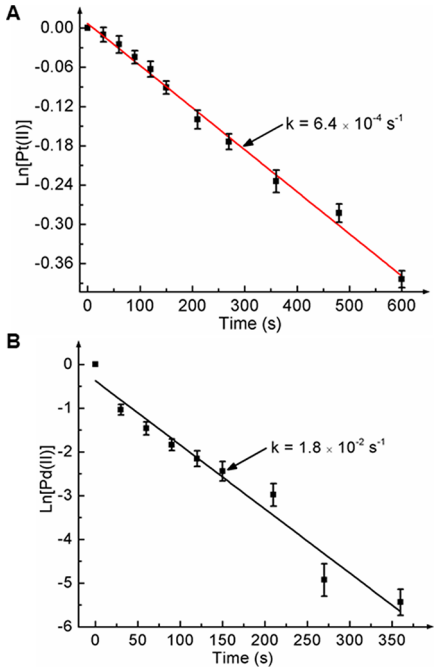


**Figure 4.** Quantitative analysis of the reduction kinetics involved in the standard synthesis of Pd@$Pt_{1L}$ octahedral nanocrystals. Plots of (A) ln[Pt(II)] and (B) ln[Pd(II)] as a function of reaction time giving straight lines whose slopes correspond to the pseudo-first-order rate constants. Note that the concentrations used to construct these plots were normalized to the initial concentration.

0.036. Combined with the initial concentrations of Pt(II) ($3.80 \times 10^{-3}$ M) and Pd(II) ($1.30 \times 10^{-2}$ M), the corresponding initial reduction rate of the Pt(II) precursor ($2.40 \times 10^{-6}$ M $s^{-1}$) was estimated to be almost 2 orders of magnitude (1:98) slower than that of the Pd(II) precursor ($2.34 \times 10^{-4}$ M $s^{-1}$). Taken together, it can be concluded that it is the drastic difference in initial reduction rate that led to the formation of a core−shell structure. This study offers another example to qualitatively demonstrate that the structure of the products can be controlled by manipulating the reduction kinetics, especially the initial reduction rate.

Figure 5A schematically illustrates our proposed mechanism to account for the formation of the Pd@$Pt_{1L}$ core−shell octahedra. Upon heating to 160 °C, the strong reducing power associated with the mixture of AA and EG can quickly reduce the Pd(II) precursor to the elemental form. According to the mechanism proposed by LaMer and Dinegar, the Pd atoms will start to aggregate to generate small clusters (i.e., nuclei) through a homogeneous nucleation process once their concentration has reached the level of supersaturation.[44] Afterward, the nuclei will grow into Pd nanocrystals with increasingly enlarged sizes until the precursor is depleted. According to the result from a previous study,[45] an initial reduction rate around $2.34 \times 10^{-4}$ M $s^{-1}$ should lead to the formation of single-crystal seeds, typically in the form of truncated octahedra (or the so-called Wulff polyhedra) encased by a mix of {111} and {100} facets. Because the truncated octahedron has a nearly spherical shape and thus the smallest ratio between the surface area and volume, the total surface free energy will be minimized.[46] This result is supported by the shape and composition evolution processes shown in Figure 2A and Figure 3. In contrast to the Pd(II) precursor, the Pt(II) precursor was reduced at a much slower rate under the same experimental conditions because of the

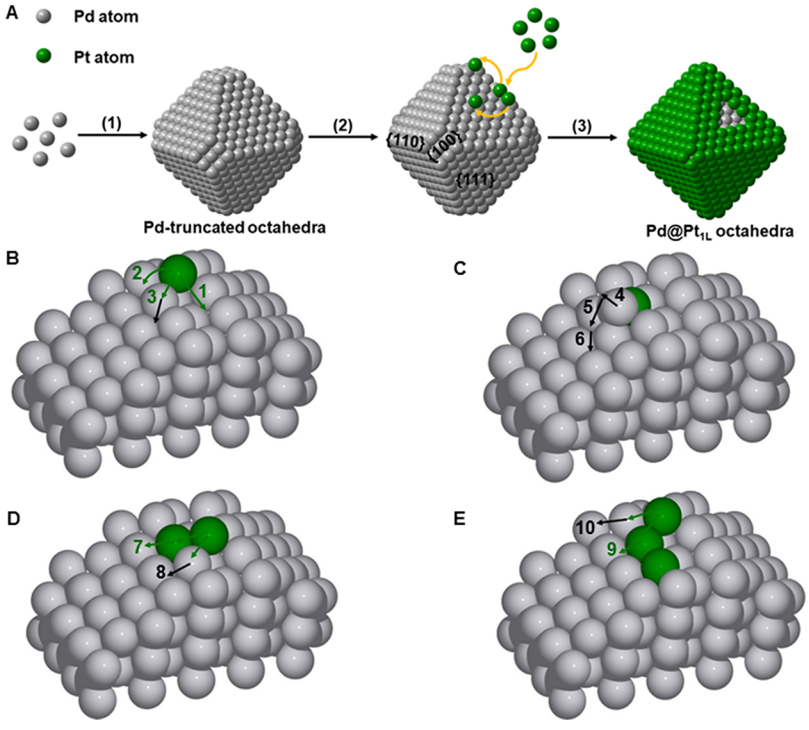


**Figure 5.** (A) Schematic illustration of the growth mechanism of Pd@$Pt_{1L}$ octahedral nanocrystals: (1) nucleation and growth of Pd octahedra with truncation at the corners; (2) selective deposition of Pt atoms on the edges of the Pd truncated octahedra; (3) surface diffusion of the deposited Pt atoms to generate Pd@$Pt_{1L}$ octahedra with sharp corners. (B−E) DFT calculated pathways for Pt and Pd diffusion across the edge model: green and black arrows represent diffusion (via hopping or substitution) of a Pt and a Pd atom, respectively.



DOI: 10.1021/acs.chemmater.8b04756
Chem. Mater. 2019, 31, 1370−1380

**Table 1. Calculated Activation Energy Barriers ($E_a$) and Diffusion Energies ($\Delta E$) for the Diffusion Processes Involving Pt and Pd Atoms Depicted in Figure 5B–E[a]**

| pathway | description | $E_a$ | $\Delta E$ |
|---|---|---|---|
| 1 | Pt atom hops from one {110} hollow site to another | 0.57 | 0.00 |
| 2 | Pt atom at a {110} hollow site hops above the Pd trough onto an fcc site on the adjacent {111} terrace | 1.59 | 0.83 |
| 3 | Pt atom at a {110} hollow site substitutes a neighboring Pd trough atom, thus pushing it onto an fcc site on the adjacent {111} terrace | 0.66 | 0.37 |
| 4 | Pd atom hops away from the {110} edge across the {111} terrace from an fcc to an hcp site | 0.06 | 0.02 |
| 5 | Pd atom hops away from the {110} edge across the {111} terrace from the previous hcp to another fcc site | 0.25 | 0.17 |
| 6 | Pd atom hops away from the {110} edge across the {111} terrace from the previous fcc to another hcp site | 0.12 | 0.07 |
| 7 | Pt atom in a {110} hollow site substitutes a neighboring Pt trough atom, thus pushing it onto an fcc site on the adjacent {111} terrace | 1.08 | 0.80 |
| 8 | Pt atom in a {110} hollow site substitutes a second Pd trough atom, thus pushing it onto an fcc site on the adjacent {111} terrace | 0.82 | 0.50 |
| 9 | Pt atom in a {110} hollow site substitutes a neighboring Pt trough atom, thus pushing it onto an fcc site on the adjacent {111} terrace | 1.09 | 0.76 |
| 10 | Pt atom in a {110} hollow site substitutes a third Pd trough atom, thus pushing it onto an hcp site on the adjacent {111} terrace | 0.91 | 0.51 |

[a]All energies are in eV.

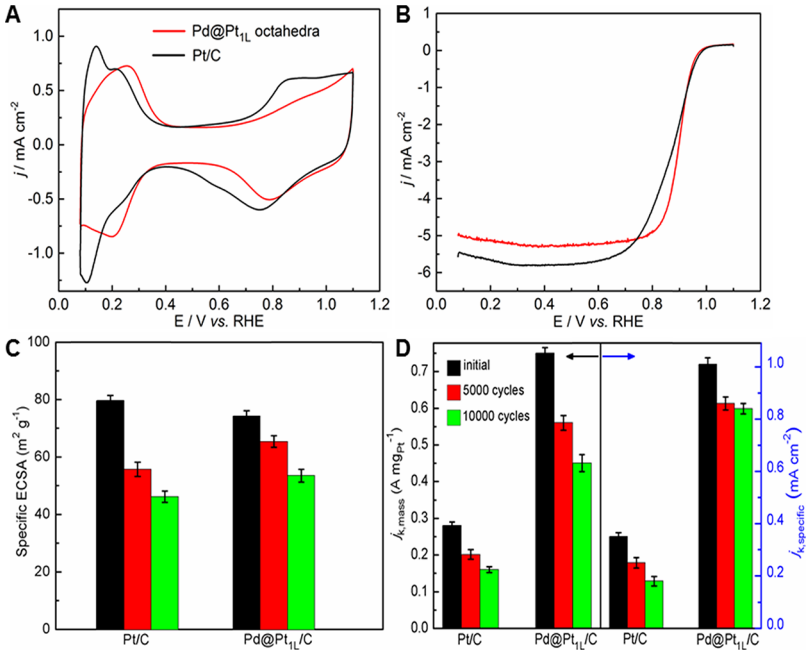


**Figure 6.** Electrochemical properties of the carbon-supported Pd@$Pt_{1L}$ octahedra, benchmarked against the Pt/C catalyst. (A) CVs of the catalysts in a $N_2$-saturated $HClO_4$ solution at room temperature. (B) Positive-going ORR polarization curves of the catalysts in an $O_2$-saturated $HClO_4$ solution. Durability tests for the carbon-supported Pd@$Pt_{1L}$ octahedra and the Pt/C catalyst. The comparison is based on (C) the specific ECSA and (D) the mass and specific ORR activity at 0.9 $V_{RHE}$ for the catalysts before and after the accelerated durability test. The color scheme specified in panel (D) applies to panel (C).

strong complexation between $Pt^{2+}$ and acetylacetone ligand. As the Pt(II) precursor was gradually reduced, the Pt atoms were deposited on the edges of the Pd core owing to a small lattice mismatch of 0.77% between Pt and Pd, as well as the lower coordination numbers at the edges.[10,47] In particular, the growth mainly occurred along the <110> directions in the initial stage of the synthesis because the surface energy of {110} facets is greater than that of {111} ones.[47,48] Afterward, the deposited Pt atoms diffused to side faces and corners at the elevated temperature, leading to the production of Pd@$Pt_{1L}$ core–shell octahedra.

To further understand the mechanism responsible for the formation of a core–shell structure, we performed a detailed DFT study of the diffusion of Pt and Pd atoms on an edge model in which two {111} terraces are joined with a {110} edge (see Figure S3). This study is summarized in Figure 5B–E and Table 1. We calculated the surface energies of the three Pd facets and found that their order went by Pd{110} > Pd{100} > Pd{111}. Given that Pd{110} has the highest surface energy among the three facets, the {110} edges should represent a preferable landing spot for the Pt atoms from solution. Therefore, we start with a Pt atom deposited on a {110} hollow site on the edge of the Pd seed (see Figure 5B). There are a few possible diffusion paths for the Pt atom to follow; the easiest is the diffusion of the Pt atom along the edge (path 1 in Figure 5B), with an activation energy barrier of 0.57 eV. To escape this edge, however, the Pt atom has to hop over the surrounding Pd atoms onto the adjacent terrace (path 2) or substitute one of the surrounding Pd atoms while pushing the Pd atom onto the terrace (substitution; path 3). While hopping (path 2) is highly activated with a 1.59 eV activation energy barrier, substitution (path 3) has an activation energy barrier of only 0.66 eV. Furthermore, substitution is 0.46 eV less endothermic than the hopping mechanism. Together, these quantities confirm that substitution will be the decisive mechanism for diffusion from edges to terraces. The diffusion of the displaced Pd atom across the terrace and away from the edge proceeds easily with barriers below 0.30 eV (paths 4–6 in


DOI: 10.1021/acs.chemmater.8b04756
Chem. Mater. 2019, 31, 1370–1380

Figure 5C and Table 1). Assuming that this displaced Pd atom has diffused away from the edge, we deposit a second Pt atom on a {110} hollow site (see Figure 5D). We already know that hopping to the terrace is not competitive, and therefore, the question as to the preferred diffusion path of the newly deposited Pt atom becomes whether such a Pt atom would rather displace a Pt or a Pd atom from the edge to the terrace, as conveyed by paths 7 and 8, respectively. We find that path 8 is less endothermic than path 7 by 0.30 eV and has an activation energy barrier of 0.82 eV, that is, 0.26 eV lower than path 7. Therefore, a newly deposited Pt atom would rather displace a Pd atom to occupy its position and sit next to another Pt atom on the edge. This process is repeated again in Figure 5E (assuming that the displaced Pd atom has diffused away from the edge), and similarly, we calculate that Pt would substitute a Pd atom (path 10) instead of another Pt atom (path 9). These results strongly suggest that the as-synthesized Pd@$Pt_{1L}$ core−shell octahedra should have a slightly mixed surface composition. At later stages of the synthesis, the newly deposited Pt atoms will only find Pt atoms at the edge to substitute, thus finally coating the seed terraces with a Pt overlayer. Like Pd, a Pt atom hopping across the terraces away from the edges is expected to be very easy (calculated activation energy barrier, assuming pure Pd seeds, is less than 0.20 eV). Finally, it is worth noting that all activation energy barriers tabulated in Table 1 are surmountable at the synthesis temperature of 160 °C. A slightly mixed surface composition for the as-synthesized Pd@$Pt_{1L}$ core−shell octahedra is also supported by the EDX line scans of Figure 1F.

We used the RDE method to characterize the ORR performance of the catalyst based on the Pd@$Pt_{1L}$ core-shell octahedra (synthesized in a continuous-flow reactor), with a commercial Pt/C catalyst serving as a reference. Prior to electrochemical measurements, the core−shell octahedra were deposited on a carbon support to obtain a Pd@$Pt_{1L}$/C catalyst (Figure S5). Through ICP-MS analysis, we confirmed that the Pd/Pt molar ratio for the Pd@$Pt_{1L}$/C catalyst was almost identical to the value of the Pd@$Pt_{1L}$ octahedra before acid treatment (3.52 vs 3.53). The TEM and ICP-MS results suggest that both the shape and composition of the Pd@$Pt_{1L}$/C catalyst were maintained during the treatment with acetic acid. Figure 6A compares the CVs recorded from the Pd@$Pt_{1L}$/C and Pt/C catalysts in the potential range of 0.08−1.10 $V_{RHE}$. From the average charges associated with hydrogen adsorption and desorption in the range of 0.08−0.43 V, the ECSAs of these two catalysts were obtained and then normalized to the amounts of Pt in the samples, generating specific ECSAs. Although the Pd@$Pt_{1L}$ octahedra had an overall size more than twice greater than that of the Pt nanoparticles in the Pt/C, the specific ECSA of the Pd@$Pt_{1L}$/C was on a par with that of the Pt/C (74.3 vs 79.6 $m^2\ g^{-1}_{Pt}$). These results confirm that the utilization efficiency of Pt atoms could indeed be increased by depositing them as an ultrathin shell on Pd nanocrystals.

Figure 6B shows the positive-going ORR polarization curves recorded from the two catalysts, from which we could derive the kinetic currents using the Koutecky−Levich equation and then normalize the values to the ECSA and Pt (or Pt + Pd) mass to obtain the specific and mass activities (i.e., $j_{k,specific}$ and $j_{k,mass}$). The results are plotted in Figure S6A,B. As expected, both the specific and mass activities of the Pd@$Pt_{1L}$/C catalyst were enhanced in comparison with those of the commercial Pt/C in the potential region of 0.86−0.94 V. Specifically, the specific activity (1.01 mA $cm^{-2}$) of the Pd@$Pt_{1L}$/C catalyst at 0.9 $V_{RHE}$ showed an enhancement of almost 3-fold when benchmarked against the Pt/C (0.35 mA $cm^{-2}$). We believe that the enhancement in specific activity mainly comes from the ligand effect, in addition to the compressive strain arising from the lattice mismatch between Pt and Pd.[19,49−51] At 0.9 $V_{RHE}$, the mass activity of the Pd@$Pt_{1L}$/C catalyst was about 0.75 A $mg^{-1}_{Pt}$, almost 3 times as high as that of the Pt/C (0.28 A $mg^{-1}_{Pt}$). In this case, the enhancement in mass activity should directly come from the extremely high utilization efficiency of Pt atoms for the Pd@$Pt_{1L}$ octahedral nanocrystals.

As shown in Figure 6C,D, the Pd@$Pt_{1L}$/C catalyst also exhibited excellent durability. The specific ECSA of the Pd@$Pt_{1L}$/C catalyst dropped less than 12% after 5000 cycles of accelerated durability tests at room temperature. In comparison, the specific ECSA of the Pt/C catalyst decreased by almost 30%. Even after 10000 cycles, the specific ECSA of the Pd@$Pt_{1L}$/C catalyst was retained at 72% of its original value, while the specific ECSA of the Pt/C catalyst only held 58% of its initial value. More specifically, Pd@$Pt_{1L}$/C catalyst still had a mass activity of 0.56 A $mg^{-1}_{Pt}$ after 5000 cycles of durability test. After 10000 cycles, the mass activity showed a slight drop to become 0.45 A $mg^{-1}_{Pt}$. Remarkably, this value was still about twice that of the mass activity of the Pt/C in the pristine state. According to a recent report, Pt atoms could be oxidized and dissolved from the Pt counter electrode and then redeposited on the working electrode during the electrocatalytic process.[52] As a result, additional Pt nanoparticles are expected to form on the carbon support during the durability test. On the basis of the TEM images shown in Figures S5 and S7, however, no additional Pt nanoparticles were observed on the carbon support for the Pd@$Pt_{1L}$ octahedra after the durability test. In this case, the number of Pt atoms dissolved from the counter electrode might be too little to nucleate and then grow into a separate population of observable nanoparticles. Alternatively, the small number of Pt atoms from the counter electrode should favor deposition on the existing Pd@$Pt_{1L}$ octahedra. However, because of the shape transformation during the durability test (see below), it was challenging to clearly resolve the possible deposition of additional Pt atoms onto the Pd@$Pt_{1L}$ octahedra.

During the durability test, some of the Pd@$Pt_{1L}$ octahedra were found to evolve into spherical particles with diameters in the range of 5−6 nm instead of generating a cage-like structure (Figure S7). This result is somewhat different from what was reported for Pd@Pt core−shell nanocrystals in the literature.[14] We believe the difference can be largely attributed to the disparity in particle size. The Pd@$Pt_{nL}$ ($n \geq 2$) octahedral nanocrystals reported in our early work were larger than 15 nm in size.[14] In contrast, the overall size of the Pd@$Pt_{1L}$ octahedral nanocrystals reported in the present work was much smaller, around 6 nm. As such, when the Pd cores were selectively dissolved and leached out during the repeated cycles, the remaining Pt atoms tended to migrate to form solid spherical particles in an effort to reduce the total energy of the system. This argument is consistent with what was reported in the literature.[9] Because of the selective dissolution of Pd atoms from the core, the proportion of {111} facets on the particle's surface dropped and the size slightly decreased relative to the sample before the durability test. As a result, both the specific ECSA and mass activity decreased.

We seek here to rationalize the high stability of the Pd@$Pt_{1L}$ octahedra. The calculated minimum energy adsorption


DOI: 10.1021/acs.chemmater.8b04756
Chem. Mater. 2019, 31, 1370−1380

configurations of O and OH on Pd@$Pt_{1L}$ core−shell octahedra slab models are given in Table S1, while the free energies of protonation of O and OH on all surfaces studied are given in Table S2. Despite the propensity of Pt to segregate to the subsurface layer in vacuum, O and OH are most stabilized on a mixed-composition surface layer model (50 and 25% Pt for 0.25 ML of O and OH, respectively) in which O and OH are coordinated to the surface Pt atom(s), as shown in the insets of Table S1. However, a significantly mixed Pd−Pt layer (as suggested by the thermodynamics of adsorption of O and OH) should offer a deteriorated performance for ORR, as indicated by higher calculated free energies of protonation on such surfaces compared to a pure Pt layer (Table S2). We note, however, that often such compositional transformations are controlled by kinetics rather than thermodynamics. To prove this point, we calculated the activation energy barriers for Pd−Pt atom exchange at the interface between the Pd body and the top layer in our slab models, up to 25% Pt composition of the top surface layer. Too high barriers for these swapping processes would explain the durability of the Pd@$Pt_{1L}$ octahedra. The results are given in Table S3 for slabs under vacuum and 0.25 ML of either O or OH. The activation energy barriers are indeed very high (>2 eV for most cases) for all systems studied. We further repeated this study, albeit in the presence of a single subsurface vacancy, in which one Pd atom was omitted from the first subsurface layer. We have previously shown that Pd octahedra are seeded during synthesis with a significant density of subsurface vacancies[35] and these vacancies could only proliferate at prolonged dissolution of Pd. The calculated activation energy barriers tabulated in Table S4 for this scenario are smaller than those for the case where there were no subsurface vacancies but are not small enough to readily occur at room temperature. This trend indicates that activation energy barriers could fall even lower in the presence of a bigger ensemble of subsurface vacancies, which is possible with the continuous dissolution of Pd at prolonged operation, thus bringing down the ORR activity. We note that this Pd dissolution process is readily initiated, given the slightly mixed top layer composition, as described earlier. Nevertheless, the high barriers reported in this study indicate that significant Pd−Pt swapping among the top two layers cannot occur on a wide scale, thus explaining the durability of the Pd@$Pt_{1L}$ octahedra.

## CONCLUSIONS

In summary, we have demonstrated a facile protocol for the one-pot synthesis of Pd@Pt core−shell octahedra with ultrathin skins that are only one atomic layer in thickness. Our kinetic analysis suggests that the formation of such a core−shell structure in one pot is mainly enabled by the large difference between the initial reduction rates of the Pd(II) and Pt(II) precursors involved in the synthesis. Specifically, the Pd(II) precursor is reduced in the initial stage to generate Pd truncated octahedra, followed by the reduction of the Pt(II) precursor for the deposition of Pt atoms as an ultrathin shell on each Pd nanocrystal. Our electrochemical measurements demonstrate that the Pd@$Pt_{1L}$ octahedral nanocrystals have greatly enhanced activity and durability toward ORR when compared with a state-of-the-art Pt/C catalyst. After 10000 cycles of accelerated durability tests, the Pd@$Pt_{1L}$ octahedral nanocrystals still have a mass activity of about twice that of the pristine Pt/C catalyst. More importantly, we have also demonstrated the use of continuous-flow reactors for potentially scaling up the production of the core−shell nanocrystals in high quality and with good uniformity. The success of this synthesis demonstrates that one can manipulate the reaction kinetics of the precursors to develop bimetallic nanocrystals with enhanced performance toward ORR and other reactions. This strategy can be potentially extended to other metals and even other types of inorganic materials. Our DFT calculations also offer atomic scale explanations of experimentally observed behaviors at three different occasions: (1) the synthesis results in a slightly mixed surface layer composition due to the preference of deposited Pt atoms to substitute Pd at the edges, (2) more extensive Pt−Pd mixing of the surface layer is thermodynamically preferred but results in deteriorated ORR activities, thus explaining the fundamental reason behind the loss of activity at prolonged operation, and (3) the calculated activation energy barriers for Pd−Pt swapping to enrich the surface layer with more Pd are prohibitive, thus indicating that such processes will be limited and in turn rationalizing the high stability of the Pd@$Pt_{1L}$ octahedra. The extensive insights gained through DFT indicate the promise of combining precise synthesis, accurate characterization, and kinetic measurements with representative DFT models to gain an appreciation of the full picture of materials synthesis and catalysis at the atomic scale.

## ASSOCIATED CONTENT

### Supporting Information

The Supporting Information is available free of charge on the ACS Publications website at DOI: 10.1021/acs.chemmater.8b04756.

Photograph showing the setup used for the continuous synthesis of Pd@$Pt_{1L}$ octahedra; TEM image of the Pd@$Pt_{1L}$ octahedral nanocrystals synthesized in continuous-flow reactors; images of the edge model; TEM images of the Pd@$Pt_{1L}$/C octahedra catalysts; plots of the specific and mass ORR activities; TEM image of the Pd@$Pt_{1L}$/C octahedra catalyst after accelerated durability test (PDF)

## AUTHOR INFORMATION


### Corresponding Authors

*E-mail: manos@engr.wisc.edu (computational work) (M.M.).
*E-mail: younan.xia@bme.gatech.edu (experimental work) (Y.X.).

### ORCID

Ming Zhou: 0000-0002-2708-0501
Ahmed O. Elnabawy: 0000-0002-8911-1916
Zachary D. Hood: 0000-0002-5720-4392
Miaofang Chi: 0000-0003-0764-1567
Manos Mavrikakis: 0000-0002-5293-5356
Younan Xia: 0000-0003-2431-7048

### Author Contributions

§M.Z., H.W., and A.O.E. contributed equally to this work.


### Notes

The authors declare no competing financial interest.

## ACKNOWLEDGMENTS

This work was supported in part by an NSF joint grant (CHE-1505441) to Georgia Tech and UW-Madison, an NSF grant (CMMI-1634687) to Georgia Tech, and startup funds from Georgia Tech. As visiting Ph.D. students from Chongqing



DOI: 10.1021/acs.chemmater.8b04756
Chem. Mater. 2019, 31, 1370−1380

University and Donghua University, respectively, M.Z. and H.W. were also partially supported by the China Scholarship Council (CSC). Z.D.H. gratefully acknowledges support from the National Science Foundation Graduate Research Fellowship under grant no. DGE-1148903 and the Georgia Tech-ORNL Fellowship. A portion of this research was completed at the Center for Nanophase Materials Sciences, which is a DOE Office of Science User Facility. Calculations were performed at supercomputing centers located at the Environmental Molecular Sciences Laboratory, which is sponsored by the DOE Office of Biological and Environmental Research at Pacific Northwest National Laboratory; the Center for Nanoscale Materials at Argonne National Laboratory, supported by DOE contract DE-AC02-06CH11357; the National Energy Research Scientific Computing Center (NERSC), a DOE Office of Science User Facility supported by DOE contract DE-AC02-05CH11231; and the UW-Madison Center for High Throughput Computing (CHTC), supported by UW-Madison, the Advanced Computing Initiative, the Wisconsin Alumni Research Foundation, the Wisconsin Institutes for Discovery, and the National Science Foundation.

## REFERENCES

(1) Debe, M. K. Electrocatalyst Approaches and Challenges for Automotive Fuel Cells. *Nature* **2012**, *486*, 43−51.

(2) Chen, J.; Lim, B.; Lee, E. P.; Xia, Y. Shape-Controlled Synthesis of Platinum Nanocrystals for Catalytic and Electrocatalytic Applications. *Nano Today* **2009**, *4*, 81−95.

(3) Stamenkovic, V. R.; Strmcnik, D.; Lopes, P. P.; Markovic, N. M. Energy and Fuels from Electrochemical Interfaces. *Nat. Mater.* **2017**, *16*, 57−69.

(4) Wang, Y.-J.; Wilkinson, D. P.; Zhang, J. Noncarbon Support Materials for Polymer Electrolyte Membrane Fuel Cell Electrocatalysts. *Chem. Rev.* **2011**, *111*, 7625−7651.

(5) Cui, C.; Gan, L.; Heggen, M.; Rudi, S.; Strasser, P. Compositional Segregation in Shaped Pt Alloy Nanoparticles and Their Structural Behaviour During Electrocatalysis. *Nat. Mater.* **2013**, *12*, 765−771.

(6) Choi, S.-I.; Xie, S.; Shao, M.; Odell, J. H.; Lu, N.; Peng, H.-C.; Protsailo, L.; Guerrero, S.; Park, J.; Xia, X.; Wang, J.; Kim, M. J.; Xia, Y. Synthesis and Characterization of 9 nm Pt−Ni Octahedra with a Record High Activity of 3.3 A/$mg_{Pt}$ for the Oxygen Reduction Reaction. *Nano Lett.* **2013**, *13*, 3420−3425.

(7) Zhang, L.; Roling, L. T.; Wang, X.; Vara, M.; Chi, M.; Liu, J.; Choi, S.-I.; Park, J.; Herron, J. A.; Xie, Z.; Mavrikakis, M.; Xia, Y. Platinum-Based Nanocages with Subnanometer-Thick Walls and Well-Defined, Controllable Facets. *Science* **2015**, *349*, 412−416.

(8) Chen, C.; Kang, Y.; Huo, Z.; Zhu, Z.; Huang, W.; Xin, H. L.; Snyder, J. D.; Li, D.; Herron, J. A.; Mavrikakis, M.; Chi, M.; More, K. L.; Li, Y.; Markovic, N. M.; Somorjai, G. A.; Yang, P.; Stamenkovic, V. R. Highly Crystalline Multimetallic Nanoframes with Three-Dimensional Electrocatalytic Surfaces. *Science* **2014**, *343*, 1339−1343.

(9) Sasaki, K.; Naohara, H.; Choi, Y.; Cai, Y.; Chen, W.-F.; Liu, P.; Adzic, R. R. Highly Stable Pt Monolayer on PdAu Nanoparticle Electrocatalysts for the Oxygen Reduction Reaction. *Nat. Commun.* **2012**, *3*, 1115.

(10) Xie, S.; Choi, S.-I.; Lu, N.; Roling, L. T.; Herron, J. A.; Zhang, L.; Park, J.; Wang, J.; Kim, M. J.; Xie, Z.; Mavrikakis, M.; Xia, Y. Atomic Layer-by-Layer Deposition of Pt on Pd Nanocubes for Catalysts with Enhanced Activity and Durability toward Oxygen Reduction. *Nano Lett.* **2014**, *14*, 3570−3576.

(11) You, H.; Yang, S.; Ding, B.; Yang, H. Synthesis of Colloidal Metal and Metal Alloy Nanoparticles for Electrochemical Energy Applications. *Chem. Soc. Rev.* **2013**, *42*, 2880−2904.

(12) Zhang, J.; Mo, Y.; Vukmirovic, M. B.; Klie, R.; Sasaki, K.; Adzic, R. R. Platinum Monolayer Electrocatalysts for $O_2$ Reduction: Pt Monolayer on Pd(111) and on Carbon-Supported Pd Nanoparticles. *J. Phys. Chem. B* **2004**, *108*, 10955−10964.

(13) Guo, S.; Li, D.; Zhu, H.; Zhang, S.; Markovic, N. M.; Stamenkovic, V. R.; Sun, S. FePt and CoPt Nanowires as Efficient Catalysts for the Oxygen Reduction Reaction. *Angew. Chem., Int. Ed.* **2013**, *52*, 3465−3468.

(14) Park, J.; Zhang, L.; Choi, S.-I.; Roling, L. T.; Lu, N.; Herron, J. A.; Xie, S.; Wang, J.; Kim, M. J.; Mavrikakis, M.; Xia, Y. Atomic Layer-by-Layer Deposition of Platinum on Palladium Octahedra for Enhanced Catalysts toward the Oxygen Reduction Reaction. *ACS Nano* **2015**, *9*, 2635−2647.

(15) Adzic, R. R.; Zhang, J.; Sasaki, K.; Vukmirovic, M. B.; Shao, M.; Wang, J. X.; Nilekar, A. U.; Mavrikakis, M.; Valerio, J. A.; Uribe, F. Platinum Monolayer Fuel Cell Electrocatalysts. *Top. Catal.* **2007**, *46*, 249−262.

(16) Zhang, J.; Vukmirovic, M. B.; Xu, Y.; Mavrikakis, M.; Adzic, R. R. Controlling the Catalytic Activity of Platinum-Monolayer Electrocatalysts for Oxygen Reduction with Different Substrates. *Angew. Chem., Int. Ed.* **2005**, *44*, 2132−2135.

(17) Stamenkovic, V. R.; Fowler, B.; Mun, B. S.; Wang, G.; Ross, P. N.; Lucas, C. A.; Markovic, N. M. Improved Oxygen Reduction Activity on $Pt_3Ni(111)$ via Increased Surface Site Availability. *Science* **2007**, *315*, 493−497.

(18) Stamenkovic, V. R.; Mun, B. S.; Arenz, M.; Mayrhofer, K. J. J.; Lucas, C. A.; Wang, G.; Ross, P. N.; Markovic, N. M. Trends in Electrocatalysis on Extended and Nanoscale Pt-Bimetallic Alloy Surfaces. *Nat. Mater.* **2007**, *6*, 241−247.

(19) Strasser, P.; Koh, S.; Anniyev, T.; Greeley, J.; More, K.; Yu, C.; Liu, Z.; Kaya, S.; Nordlund, D.; Ogasawara, H.; Toney, M. F.; Nilsson, A. Lattice-Strain Control of the Activity in Dealloyed Core-Shell Fuel Cell Catalysts. *Nat. Chem.* **2010**, *2*, 454−460.

(20) Hunt, S. T.; Milina, M.; Alba-Rubio, A. C.; Hendon, C. H.; Dumesic, J. A.; Román-Leshkov, Y. Self-Assembly of Noble Metal Monolayers on Transition Metal Carbide Nanoparticle Catalysts. *Science* **2016**, *352*, 974−978.

(21) Wang, X.; Figueroa-Cosme, L.; Yang, X.; Luo, M.; Liu, J.; Xie, Z.; Xia, Y. Pt-Based Icosahedral Nanocages: Using a Combination of {111} Facets, Twin Defects, and Ultrathin Walls to Greatly Enhance Their Activity toward Oxygen Reduction. *Nano Lett.* **2016**, *16*, 1467−1471.

(22) Wu, J.; Qi, L.; You, H.; Gross, A.; Li, J.; Yang, H. Icosahedral Platinum Alloy Nanocrystals with Enhanced Electrocatalytic Activities. *J. Am. Chem. Soc.* **2012**, *134*, 11880−11883.

(23) Cui, C.; Gan, L.; Li, H.-H.; Yu, S.-H.; Heggen, M.; Strasser, P. Octahedral PtNi Nanoparticle Catalysts: Exceptional Oxygen Reduction Activity by Tuning the Alloy Particle Surface Composition. *Nano Lett.* **2012**, *12*, 5885−5889.

(24) Ortiz, N.; Weiner, R. G.; Skrabalak, S. E. Ligand-Controlled Co-Reduction versus Electroless Co-Deposition: Synthesis of Nanodendrites with Spatially Defined Bimetallic Distributions. *ACS Nano* **2014**, *8*, 12461−12467.

(25) Zhou, M.; Wang, H.; Vara, M.; Hood, Z. D.; Luo, M.; Yang, T.-H.; Bao, S.; Chi, M.; Xiao, P.; Zhang, Y.; Xia, Y. Quantitative Analysis of the Reduction Kinetics Responsible for the One-Pot Synthesis of Pd-Pt Bimetallic Nanocrystals with Different Structures. *J. Am. Chem. Soc.* **2016**, *138*, 12263−12270.

(26) Chen, Q.; Zhang, J.; Jia, Y.; Jiang, Z.; Xie, Z.; Zheng, L. Wet Chemical Synthesis of Intermetallic $Pt_3Zn$ Nanocrystals via Weak Reduction Reaction Together with UPD Process and Their Excellent Electrocatalytic Performances. *Nanoscale* **2014**, *6*, 7019−7024.

(27) Durieux, G.; Gerdin, M.; Moberg, C.; Jutand, A. Rate and Mechanism of the Oxidative Addition of a Silylborane to $Pt^0$ Complexes−Mechanism for the Pt-Catalyzed Silaboration of 1, 3-Cyclohexadiene. *Eur. J. Inorg. Chem.* **2008**, *2008*, 4236−4241.

(28) Gilroy, K. D.; Ruditskiy, A.; Peng, H.-C.; Qin, D.; Xia, Y. Bimetallic Nanocrystals: Syntheses, Properties, and Applications. *Chem. Rev.* **2016**, *116*, 10414−10472.

(29) Blöchl, P. E. Projector Augmented-Wave Method. *Phys. Rev. B* **1994**, *50*, 17953−17979.



DOI: 10.1021/acs.chemmater.8b04756
*Chem. Mater.* 2019, 31, 1370−1380

(30) Kresse, G.; Joubert, D. From Ultrasoft Pseudopotentials to the Projector Augmented-Wave Method. *Phys. Rev. B* **1999**, *59*, 1758−1775.
(31) Perdew, J. P.; Wang, Y. Accurate and Simple Analytic Representation of the Electron-Gas Correlation Energy. *Phys. Rev. B* **1992**, *45*, 13244−13249.
(32) Kresse, G.; Furthmüller, J. Efficient Iterative Schemes for Ab Initio Total-Energy Calculations Using a Plane-Wave Basis Set. *Phys. Rev. B* **1996**, *54*, 11169−11186.
(33) Kresse, G.; Furthmüller, J. Efficiency of Ab-Initio Total Energy Calculations for Metals and Semiconductors Using a Plane-Wave Basis Set. *Comput. Mater. Sci.* **1996**, *6*, 15−50.
(34) Haynes, W. M., Bruno, T. J., Lide, D. R. Eds. *CRC Handbook of Chemistry and Physics*, 96th ed.; CRC Press: Boca Raton, FL, 2016.
(35) Vara, M.; Roling, L. T.; Wang, X.; Elnabawy, A. O.; Hood, Z. D.; Chi, M.; Mavrikakis, M.; Xia, Y. Understanding the Thermal Stability of Palladium-Platinum Core-Shell Nanocrystals by In Situ Transmission Electron Microscopy and Density Functional Theory. *ACS Nano* **2017**, *11*, 4571−4581.
(36) Monkhorst, H. J.; Pack, J. D. Special Points for Brillouin-Zone Integrations. *Phys. Rev. B* **1976**, *13*, 5188−5192.
(37) Henkelman, G.; Uberuaga, B. P.; Jónsson, H. A Climbing Image Nudged Elastic Band Method for Finding Saddle Points and Minimum Energy Paths. *J. Chem. Phys.* **2000**, *113*, 9901−9904.
(38) Neugebauer, J.; Scheffler, M. Adsorbate-Substrate and Adsorbate-Adsorbate Interactions of Na and K Adlayers on Al(111). *Phys. Rev. B* **1992**, *46*, 16067−16080.
(39) Bengtsson, L. Dipole Correction for Surface Supercell Calculations. *Phys. Rev. B* **1999**, *59*, 12301−12304.
(40) Ruban, A. V.; Skriver, H. L.; Nørskov, J. K. Surface Segregation Energies in Transition-Metal Alloys. *Phys. Rev. B* **1999**, *59*, 15990−16000.
(41) Nørskov, J. K.; Rossmeisl, J.; Logadottir, A.; Lindqvist, L.; Kitchin, J. R.; Bligaard, T.; Jónsson, H. Origin of the Overpotential for Oxygen Reduction at a Fuel-Cell Cathode. *J. Phys. Chem. B* **2004**, *108*, 17886−17892.
(42) Greeley, J.; Rossmeisl, J.; Hellmann, A.; Nørskov, J. K. Theoretical Trends in Particle Size Effects for the Oxygen Reduction Reaction. *Z. Phys. Chem.* **2007**, *221*, 1209−1220.
(43) Luty-Błocho, M.; Pacławski, K.; Wojnicki, M.; Fitzner, K. The Kinetics of Redox Reaction of Gold(III) Chloride Complex Ions with L-ascorbic Acid. *Inorg. Chim. Acta* **2013**, *395*, 189−196.
(44) LaMer, V. K.; Dinegar, R. H. Theory, Production and Mechanism of Formation of Monodispersed Hydrosols. *J. Am. Chem. Soc.* **1950**, *72*, 4847−4854.
(45) Wang, Y.; Peng, H.-C.; Liu, J.; Huang, C. Z.; Xia, Y. Use of Reduction Rate as a Quantitative Knob for Controlling the Twin Structure and Shape of Palladium Nanocrystals. *Nano Lett.* **2015**, *15*, 1445−1450.
(46) Xia, Y.; Xiong, Y.; Lim, B.; Skrabalak, S. E. Shape-Controlled Synthesis of Metal Nanocrystals: Simple Chemistry Meets Complex Physics? *Angew. Chem., Int. Ed.* **2009**, *48*, 60−103.
(47) Wang, X.; Vara, M.; Luo, M.; Huang, H.; Ruditskiy, A.; Park, J.; Bao, S.; Liu, J.; Howe, J.; Chi, M.; Xie, Z.; Xia, Y. Pd@Pt Core-Shell Concave Decahedra: A Class of Catalysts for the Oxygen Reduction Reaction with Enhanced Activity and Durability. *J. Am. Chem. Soc.* **2015**, *137*, 15036−15042.
(48) Wang, Y.; Xie, S.; Liu, J.; Park, J.; Huang, C. Z.; Xia, Y. Shape-Controlled Synthesis of Palladium Nanocrystals: A Mechanistic Understanding of the Evolution from Octahedrons to Tetrahedrons. *Nano Lett.* **2013**, *13*, 2276−2281.
(49) Kitchin, J. R.; Nørskov, J. K.; Barteau, M. A.; Chen, J. G. Role of Strain and Ligand Effects in the Modification of the Electronic and Chemical Properties of Bimetallic Surfaces. *Phys. Rev. Lett.* **2004**, *93*, 156801−156804.
(50) Mavrikakis, M.; Hammer, B.; Nørskov, J. K. Effect of Strain on the Reactivity of Metal Surfaces. *Phys. Rev. Lett.* **1998**, *81*, 2819−2822.
(51) Wu, J.; Li, P.; Pan, Y.-T.; Warren, S.; Yin, X.; Yang, H. Surface Lattice-Engineered Bimetallic Nanoparticles and Their Catalytic Properties. *Chem. Soc. Rev.* **2012**, *41*, 8066−8074.
(52) Inzelt, G.; Berkes, B.; Kriston, Á. Two Types of Platinum Dissolution in Acid Media: An Electrochemical Nanogravimetric Study. *ECS Trans.* **2010**, *25*, 137−156.


DOI: 10.1021/acs.chemmater.8b04756
*Chem. Mater.* 2019, 31, 1370−1380